Exocytosis of the silicified cell wall of diatoms involves extensive membrane disintegration

Diede de Haan[1], Lior Aram[1], Hadas Peled-Zehavi[1], Yoseph Addadi[2], Oz Ben-Joseph[1], Ron Rotkopf[2], Nadav Elad[3], Katya Rechav[3] and Assaf Gal[1]*

[1]Department of Plant and Environmental Sciences, Weizmann Institute of Science, Rehovot, Israel

[2]Life Sciences Core Facilities, Weizmann Institute of Science, Rehovot, Israel

[3]Department of Chemical Research Support, Weizmann Institute of Science, Rehovot, Israel

*email: assaf.gal@weizmann.ac.il

Classification

Biological Science, Microbiology

Keywords

Biomineralization, Diatoms, Exocytosis, Silica deposition vesicle, Membrane dynamics

Significance Statement

Exocytosis is a fundamental process for cell metabolism, communication, and growth. During exocytosis, an intracellular vesicle fuses with the plasma membrane to release its contents. In classical exocytosis, where the exocytosed vesicles are much smaller than the cell, membrane homeostasis is maintained by recycling excess membranes back into the cell. However, an extreme case of exocytosis is the extrusion of large and rigid cell wall elements by unicellular marine algae. During this process, the cell needs to deal with a potential doubling of its plasma membrane. This study reports on a unique exocytosis mechanism used by these organisms, in which the cells cope with the geometrical and physical challenges of exocytosis by releasing a significant amount of membranes to the extracellular space.

Abstract

Diatoms are unicellular algae, characterized by silica cell walls. The silica elements are formed intracellularly in a membrane-bound silica deposition vesicle (SDV), and are exocytosed after completion. How diatoms maintain membrane homeostasis during the exocytosis of these large and rigid silica elements is a long-standing enigma. We studied membrane dynamics during cell wall formation and exocytosis in two model diatom species, using live-cell confocal microscopy, transmission electron microscopy and cryo-electron tomography. Our results show that during the formation of the mineral phase it is in tight association with the SDV membranes, which are forming a precise mold of the delicate geometrical patterns. During exocytosis, the distal SDV membrane and the plasma membrane gradually detach from the mineral and disintegrate in the extracellular space, without any noticeable endocytic retrieval or extracellular repurposing. Within the cell, there is no evidence for the formation of a new plasma membrane, thus the proximal SDV membrane becomes the new barrier between the cell and its environment, and assumes the role of a new plasma membrane. These results provide direct structural observations of diatom silica exocytosis, and point to an extraordinary mechanism in which membrane homeostasis is maintained by discarding, rather than recycling, significant membrane patches.

43 **Introduction**

44 Diatoms are a diverse group of unicellular algae characterized by silica cell walls with intricate,
45 species-specific shapes and hierarchical pore patterns (1). Despite immense morphological
46 diversity between species, most diatom cell walls have a conserved layout of two similarly shaped
47 silica 'shells' that partially overlap, like a petri-dish. Each 'shell' in itself consists of a valve and a
48 series of girdle bands. The valves usually define the shape of the cell, are richly ornamented, and
49 contain hierarchical pore patterns. The girdle bands form partially overlapping rings that surround
50 the sidewalls of the cells.

51 Diatom cell wall formation is under biological control and linked to the cell cycle (2–5).
52 Each daughter cell inherits one half of the parental cell wall and forms a second valve directly
53 after cell division. New girdle bands are formed and appended to the new valve during the growth
54 of the cell (Fig. S1). Silicification is usually an intracellular process, taking place inside a
55 membrane-bound organelle, the silica deposition vesicle (SDV) (6–8). SDVs are elongated, but
56 very thin organelles, positioned directly under the plasma membrane. Inside the SDV, the
57 chemical environment and biological regulation exert tight control over the silicification process,
58 resulting in highly specific and reproducible cell wall architectures (9–13). After intracellular
59 maturation, the silica elements are exocytosed to cover the cell surface (6, 14). Such exocytosis
60 events are exceptional in cell biology since the content of the SDV is an enormous solid structure
61 that needs to be secreted without damaging the integrity of the cell.

62 In classical exocytosis pathways, the membrane of an intracellular vesicle fuses with the
63 plasma membrane to deliver its content into the extracellular space. Homeostasis of the plasma
64 membrane can be maintained through a transient fusion that prevents the secreting vesicle from
65 integrating with the plasma membrane, or by offsetting the added membrane through
66 compensatory endocytosis (15). However, due to their large size and rigidity, the secretion of
67 diatom cell walls inflict a huge challenge to the organism. The new valve covers as much as half
68 of the total cell surface and thus the surface area of the SDV membrane is similar to the entire
69 plasma membrane, therefore, fusion with the SDV membrane would lead to an almost
70 instantaneous doubling of the plasma membrane area.

While former studies have brought forward several hypotheses for silica cell wall exocytosis in diatoms (14, 16–23; Fig. S2), significant experimental challenges have hindered further progress. On the one hand, traditional sample preparation for ultrastructural studies with electron microscopy causes artefacts like membrane shrinking and structure deformation (24). On the other hand, the advantages of light microscopy in studying the dynamic aspects of cell wall formation in living cells are limited by the low spatial resolution and scarcity of molecular biology tools for diatoms (25, 26). Due to these limitations, in situ observations of the SDV in the cellular context are sparse, and direct evidence for the nature of the silicification and exocytosis process is missing.

In this study, we investigated membrane dynamics during valve formation and exocytosis in two model diatom species, *Stephanopyxis turris* and *Thalassiosira pseudonana*, using live-cell confocal fluorescence microscopy, transmission electron microscopy (TEM) and cryo electron tomography (cryo-ET). The relatively large *S. turris* cells have easily discernible silica structures, allowing detailed observations of individual valves and the dynamic development of their architectural features using fluorescence microscopy (27, 28). In addition, using cryo-ET we obtain high-resolution 3D data of the SDV in *T. pseudonana*, at native-like conditions (29, 30). Our results indicate that valve exocytosis in both species involves disintegration of the distal membranes, accompanied by the repurposing of the proximal SDV membrane into a new plasma membrane.

Results

We investigated valve exocytosis in diatoms by studying two species, *S. turris* and *T. pseudonana* (Fig. 1). The valves of *S. turris* are capsule-shaped and have a two-layered structure. The proximal layer is thin, perforated by nano-sized pores, and on the distal side overlain by a more elevated layer that forms large polygons. The top of the polygonal layer is flattened, forming a 'T'-shape in cross-section (Fig. 1 A''). *S. turris* cells form chains that are linked through tubular linking extensions of silica that extend from the apex of the valves (Fig. 1 A, arrow). *T. pseudonana* cells are shaped as a barrel and are much smaller, the valves are discs with a diameter of about 5 µm (Fig. 1 B). Small pores perforate the silica layer that spans the area between radial ribs, and larger tubular pores, called fultoportulae, decorate the rim of the valve (Fig. 1 B') (7). Figure 1 E and F

show dividing cells during and shortly after valve formation. Newly formed valves are stained by PDMPO, a fluorescent dye that is incorporated into silica during the process of biological mineralization (31). Comparing the cell size to the size of mature valves shortly before exocytosis illustrates the enormous challenge involved in exocytosis of these rigid silica cell walls (Fig. 1 G, H).

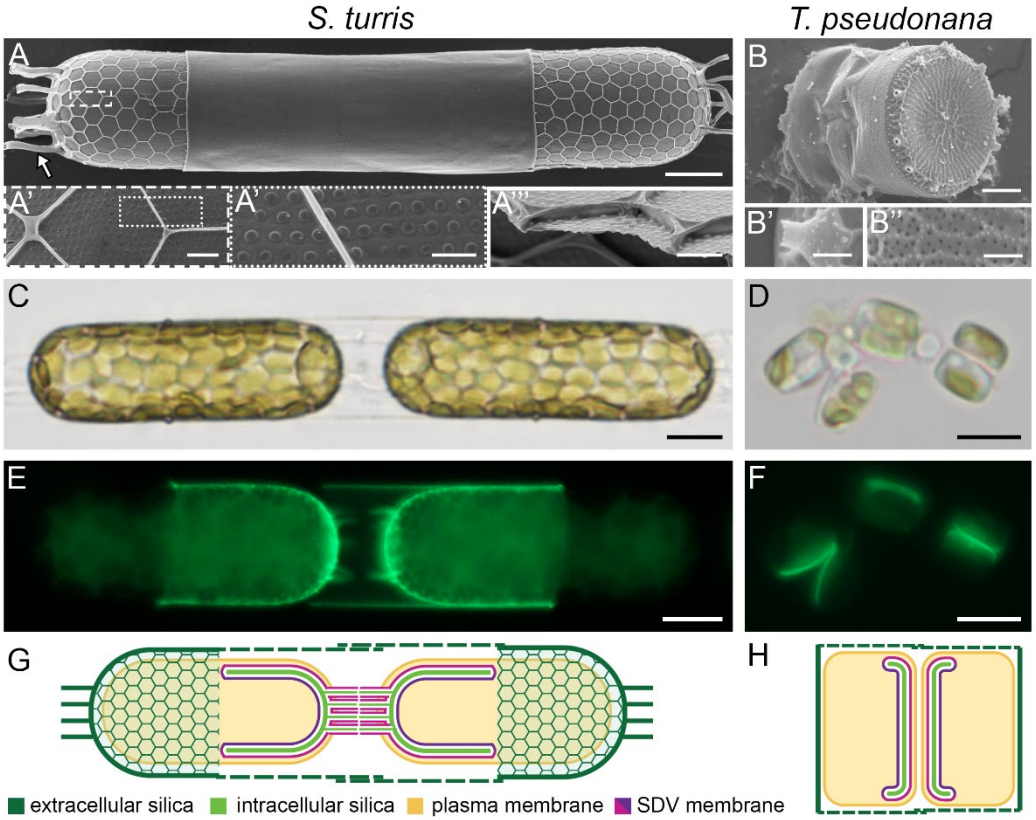

Figure 1. Cell architecture of *S. turris* (A, C, E, G) **and *T. pseudonana*** (B, D, F, H)**.** (**A-B**) SEM images. Details of the silica valve structures are shown at higher magnifications in the sub-panels. (**C-D**) Bright field light microscope images of two *S. turris* cells in a chain connected through linking extensions and several *T. pseudonana* cells at different stages during the cell cycle. (**E-F**) PDMPO fluorescence image of two different *S. turris* daughter cells during valve formation, and the same *T. pseudonana* cells as in (**D**) with new valves fluorescently stained by PDMPO. (**G-H**) Schematic of *S. turris* and *T. pseudonana* depicting the situation shortly before exocytosis of intracellularly formed valves. Scale bars: 10 µm (**A, C, E**), 5 µm (**D, F**), 1 µm (**A', A''', B**) 500 nm (**A''**), 100 nm (**B', B''**).

We studied membrane dynamics in *S. turris* using time-lapse confocal microscopy on living cells (Fig. 2). Synchronized cultures were labelled with PDMPO to track silica formation (Fig. S3), and with FM4-64 to stain the plasma membrane. FM4-64 is an amphiphilic, membrane-impermeable dye, that enters the cell only via endocytic vesicles (32, 33). During silicification, the PDMPO and FM4-64 signals are almost indistinguishable, demonstrating the close proximity of the plasma membrane to the growing silica structures within the SDV (Fig. 2 A). This is exemplified during the formation of the polygons and the linking extensions, for which the fluorescent membrane signal by itself mirrors the process of silica growth. Nevertheless, the growing tips of linking extensions are exclusively stained by the membrane dye, indicating that SDV elongation precedes silicification (Fig. 2 A, arrow).

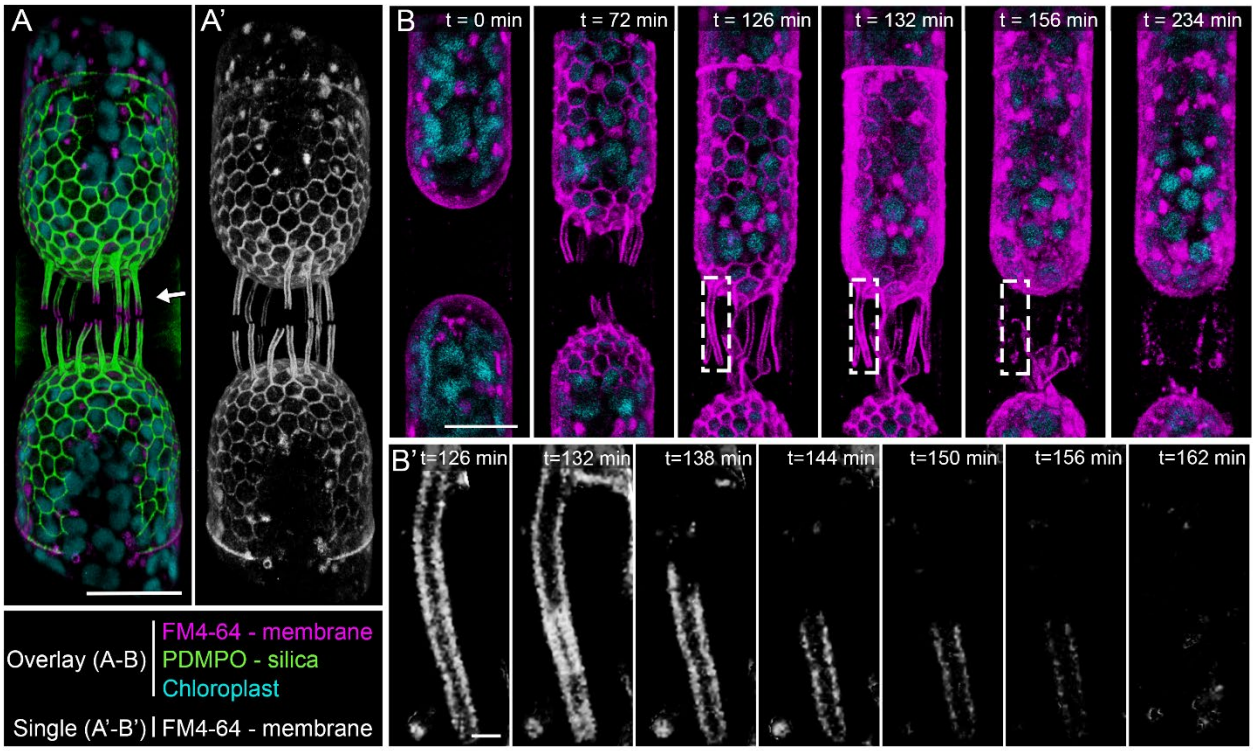

Figure 2. 3D reconstructions of time-lapse confocal fluorescence images showing coordinated silica and membrane dynamics during valve formation in *S. turris*. A, B) Overlay images of fluorescence channels. **A', B'**) Single channel FM4-64 fluorescence images. (**A-A'**) Daughter cells during valve formation. Membranes outline the growing polygons and lead the growth of linking extensions (arrow). (**B**) Snapshots from a time-lapse of daughter cells going through valve

128 formation and exocytosis. Elapsed time since start of imaging is indicated in the image. (**B'**)
129 Cropped and magnified view of a single linking extension of the cell in **B** (indicated with boxes).
130 Onset of exocytosis of the valve can be seen from t=132, after which the membrane remnants
131 around the linking process are no longer connected to the cell and gradually disintegrate. Scale
132 bars: 20 µm (**A, A'**), 10 µm (**B**), and 1 µm (**B'**).

133 We recorded a time-lapse of the membrane dynamics in *S. turris* cells going through the
134 entire process of valve formation and exocytosis (Fig. 2 B, Movie S1). Silicification starts at the cell
135 apex and advances radially. Progress of valve formation is visualized by the fluorescent plasma
136 membrane outlining the growing polygonal silica layer and linking extensions (Fig. 2 B, t=0 to
137 t=126). The onset of exocytosis, namely the loosening of the plasma membrane – SDV – silica
138 complex is evident as the labelled plasma membrane no longer sharply outlines the polygons (Fig.
139 2 B, t=132). At the same time point, we observe an enhancement of the fluorescent signal (Fig.
140 S4), likely due to fusion between the plasma and SDV membranes that exposes the SDV lumen to
141 the surrounding media, from which free FM4-64 can infiltrate and stain the SDV membrane
142 additionally to the plasma membrane. Nevertheless, the limited resolution of fluorescence
143 microscopy does not allow to spatially resolve the interplay between SDV and plasma membranes
144 before and after exocytosis (Fig. S5).

145 The linking extensions of *S. turris* present a unique opportunity to investigate the
146 exocytosis process as the old plasma membrane surrounds these long structures before
147 exocytosis, but after exocytosis, the new plasma membrane is only at their base. The FM4-64
148 signal around the linking extensions is continuous during their growth, but after the extensions
149 reached their full size the fluorescent signal changes to interrupted patches that gradually
150 disappear (Fig. 2 B, t=156 and t=234). In some cases, the membranes surrounding a linking
151 extension are clearly no longer connected to the cell body (Fig. 2 B'). This labelling pattern, in
152 which patches of stained membranes are disconnected from the cell, is very different from the
153 expectation for a classical exocytosis process where stained membranes should be withdrawn
154 and recycled inside the cell. It is important to note that FM4-64 is only transiently attached to the

155 membranes and is present in the medium throughout the experiment. Therefore, it labels only
156 structurally-intact membranes and when a membrane is disintegrated it will no longer label the
157 malformed debris. Thus, these observations point to a scenario where major fractions of the distal
158 membranes are completely detached from the main cell surface, gradually disintegrate, and lose
159 their fluorescent labeling in the extracellular space between recently divided daughter cells.

160 To observe the same process at ultrastructural resolution we prepared dividing *S. turris*
161 cells for TEM analysis. In short, synchronized cells were vitrified using high-pressure freezing and
162 subsequently freeze-substituted and embedded in resin. This results in an optimal combination
163 of near-to-native state preservation of subcellular structures paired with the ability of high-
164 throughput TEM imaging at room temperature. The TEM images of *S. turris* cells prepared
165 according to this procedure show exceptional preservation of the cellular environment and
166 notably the SDV membranes and inorganic contents (Fig. S6).

167 We acquired hundreds of images from 227 cells at different stages of the cell cycle, and
168 by categorizing and sorting these images, we reconstructed a timeline of valve formation and
169 exocytosis in *S. turris* (Fig. 3). Cells with an SDV containing a growing valve were classified as being
170 at the stage of valve formation (n=61, examples presented in Fig. 3 A-B''). At these stages three
171 lipid bilayers, the proximal and distal SDV membranes, as well as the plasma membrane, can be
172 clearly distinguished. The distal SDV membrane is in very close proximity to the plasma
173 membrane, with a distance of only 10-30 nm (Fig. 3 A'' inset). During early valve formation, the
174 SDV extends only as far as silica deposition has advanced (Fig. 3 A''). As silica precipitation
175 proceeds radially, the SDV expands with it. After formation of the porous base layer, the polygonal
176 layer is formed on its distal side (Fig. 3 B-B'', arrow). During the entire silicification process, the
177 SDV membrane tightly delineates the growing valve, forming a highly confined space in which the
178 silica morphology is under control of the SDV membrane. The valve reaches its final morphology
179 while it is still fully enclosed in the SDV, we observed 23 cells with an intact SDV containing a fully
180 mature valve (Fig. 3 C-C'').

181

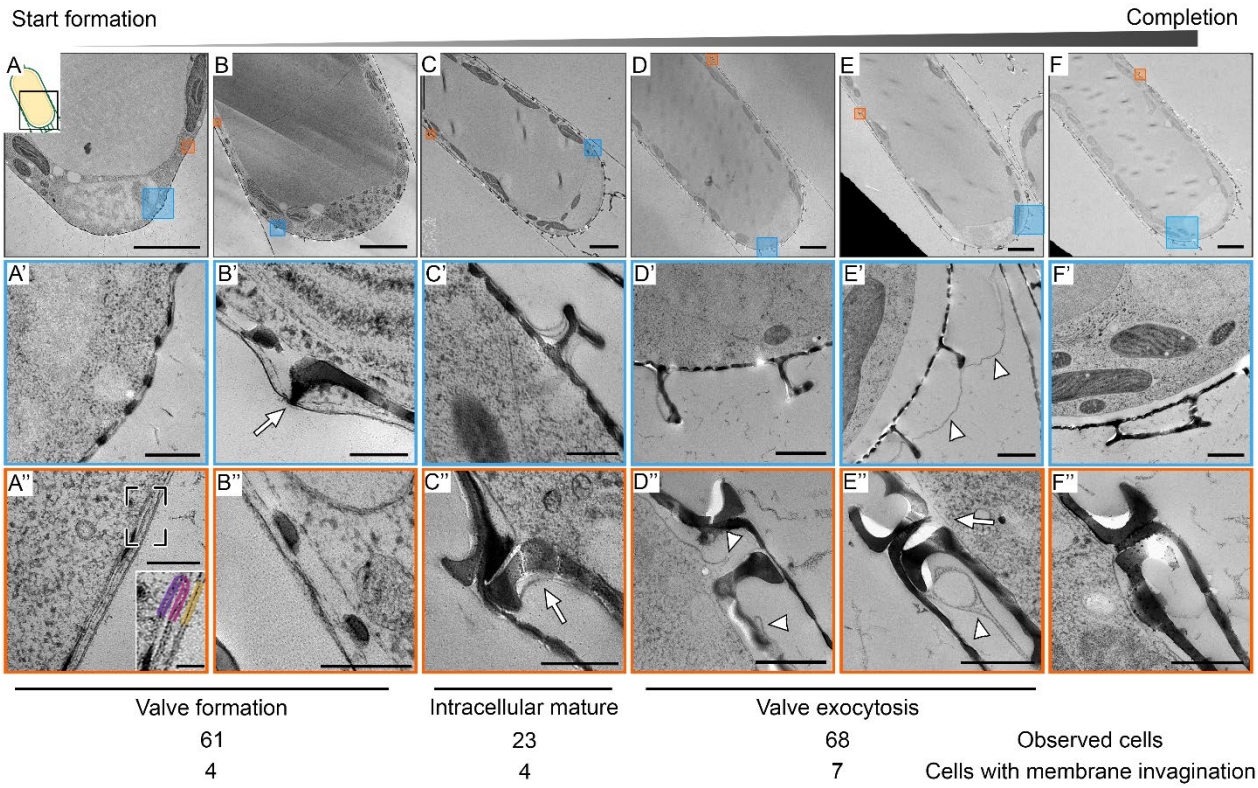

Figure 3. TEM images showing sequential stages of valve formation and exocytosis in *S. turris*. Top row shows a representative image of each stage, with higher magnification views of the boxed areas in the rows below. (**A**) Valve formation starts at the apex of the cell. (**A'**) Growing silica inside the SVD that is located directly under the plasma membrane. (**A''**) The SDV ends at the growing silica edge. The inset shows the bilayers of the proximal (purple) and distal (pink) SDV and the plasma membrane (yellow) in higher magnification. (**B**) Later during valve formation, (**B'**) the polygonal layer (arrow) is formed on top of the base layer, and (**B''**) the growing edge of the new valve reaches the rim of the parental valve. (**C**) Silicification of the new valve is completed while it is still fully enclosed in the SDV. Mature valves can be recognized by (**C'**) the fully formed and flattened polygonal layer and (**C''**) pronounced hook shape at the valve rim (arrow). (**D**) At the onset of exocytosis, (**D'**) membranes still surround most parts of the new valve, (**D''**) but they no longer form a complete enclosure (arrowheads). (**E**) Shortly after exocytosis, (**E'**) distal membranes lose their structural integrity (arrowheads), and (**E''**) the plasma membrane is now continuous (arrow) under the new valve. (**F-F''**) After completion of exocytosis, there are no traces left of the distal membrane remnants. Below the images, a table summarizes the number of cells

197 observed in each developmental stage and the number of cases when membrane invaginations
198 was present (see details in Fig. S7 and main text). Scale bars represent 5 μm (**A, B, C, D, E, F**), 1
199 μm (**D', E', F'**), 500 nm (**A', C', C'', D'', E'', F''**), 200 nm (**A'', B', B'', C'** inset) and 50 nm (**A'' inset**).

200 In images of 68 cells, we observed a mature valve that is surrounded by SDV membranes
201 with some discontinuities, i.e. the SDV does not form a complete enclosure. Based on this
202 structural information we define these cells as undergoing exocytosis. These membrane
203 discontinuities can be very local, while the majority of the valve is still tightly enclosed by the SDV
204 (Fig. 3 D-D''). At a later stage, the membrane ultrastructure changes dramatically. The tight
205 delineation of the distal SDV and plasma membrane around the valve loosens, and we observe
206 deterioration of the structural integrity of the distal membranes (Fig 3. E-E''). The membrane at
207 the proximal side of the valve is now continuous with the plasma membrane under the parental
208 valve (Fig. 3 E'' arrow). At the end of the exocytosis process, the new valves can be recognized
209 due to their position under the parental girdle bands, while no visible traces of the membranes
210 are seen outside the cytoplasm (Fig. 3 F-F'').

211 We analyzed the microscopy data of the membrane proximal to the newly formed valves
212 in order to identify possible signs of endocytic membrane retrieval that might be associated with
213 recycling the SDV membranes. We observed 7 occasions of membrane invaginations in cells at
214 the exocytosis stage. The size of these invaginations varies from 0.5 μm to 3 μm (Fig. S7).
215 However, such invaginations were detected at all stages of valve formation and exocytosis with
216 similar occurrence ($X^2_{(df=2,\ N=152)} = 2.23$, $p = .327$), and thus cannot be correlated to membrane
217 recycling after exocytosis. Overall, the TEM data is in agreement with the live-cell imaging,
218 suggesting that during valve exocytosis the distal membranes disintegrate extracellularly without
219 signs of retrieval, while the only visible membrane proximal to the new valve is the proximal SDV
220 membrane.

221 In order to visualize the cellular organization as close as possible to the native state, we
222 acquired cryo-ET data from *T. pseudonana* cells undergoing valve exocytosis. The smaller size of
223 these cells makes them suitable for the needed sample preparation steps for imaging with cryo-
224 ET. In short, we vitrified synchronized *T. pseudonana* cells using plunge freezing, prepared thin

225 lamellae using a focused ion beam and then collected electron tomograms under cryogenic
226 conditions (30, 34). Out of the 59 pairs of daughter cells that were imaged, 15 were during or
227 shortly after valve exocytosis, i.e. before exocytosis of the first set of girdle bands. Four of those
228 were during the early stages of exocytosis, with the new valve only partly covered by SDV
229 membranes (Fig 4 A-D).

230 Figure 4 A and C show tomograms of different locations of the same pair of slightly
231 unsynchronized daughter cells, the left one shortly before exocytosis and the right one during
232 exocytosis. The valve on the left side is still completely enclosed within the SDV, while the valve
233 on the right side is already exposed to the extracellular space through discontinuities in the
234 coverage by the distal membranes. In both cells, three lipid bilayers are discernible. In the
235 daughter cell before exocytosis the expected arrangement of membranes is seen: the plasma
236 membrane covers the whole cell and closely underneath the SDV membranes fully surround the
237 valve (Fig. 4 A-B, left side). However, during exocytosis the distal membranes have fused at
238 multiple sites, forming a network of flat membrane sacs, making the membrane on the proximal
239 side of the valve the outermost boundary of the cell (Fig. 4 A-B, right side). A similar situation is
240 observed at the valve periphery, where unconnected membranous structures are seen at the
241 distal side of the fultoportula (Fig. 4 C-D, right side).

242 In eight pairs of cells that were at later stages of exocytosis we observed large
243 membranous vesicles positioned between the recently exocytosed valves of two daughter cells
244 and their girdle bands (Fig. 4 E). In the three remaining pairs of cells with recently exocytosed
245 valves we did not observe any vesicles or membrane remnants between the two daughter cells.
246 However, in those three cells the parental girdle bands were not enclosing the daughter cells,
247 pointing to a later stage of the cell cycle, by which all extracellular debris had been degraded.
248 Notably, none of the imaged cells contained budding endocytic vesicles or a sign for the formation
249 of a new membrane underneath the valve. Therefore, the cryo-ET data suggest that *T.*
250 *pseudonana* uses the same exocytosis mechanism that we inferred from *S. turris*, where the
251 proximal SDV membrane is repurposed as a new plasma membrane and the distal membranes
252 disintegrate extracellularly (Fig. 4 F).

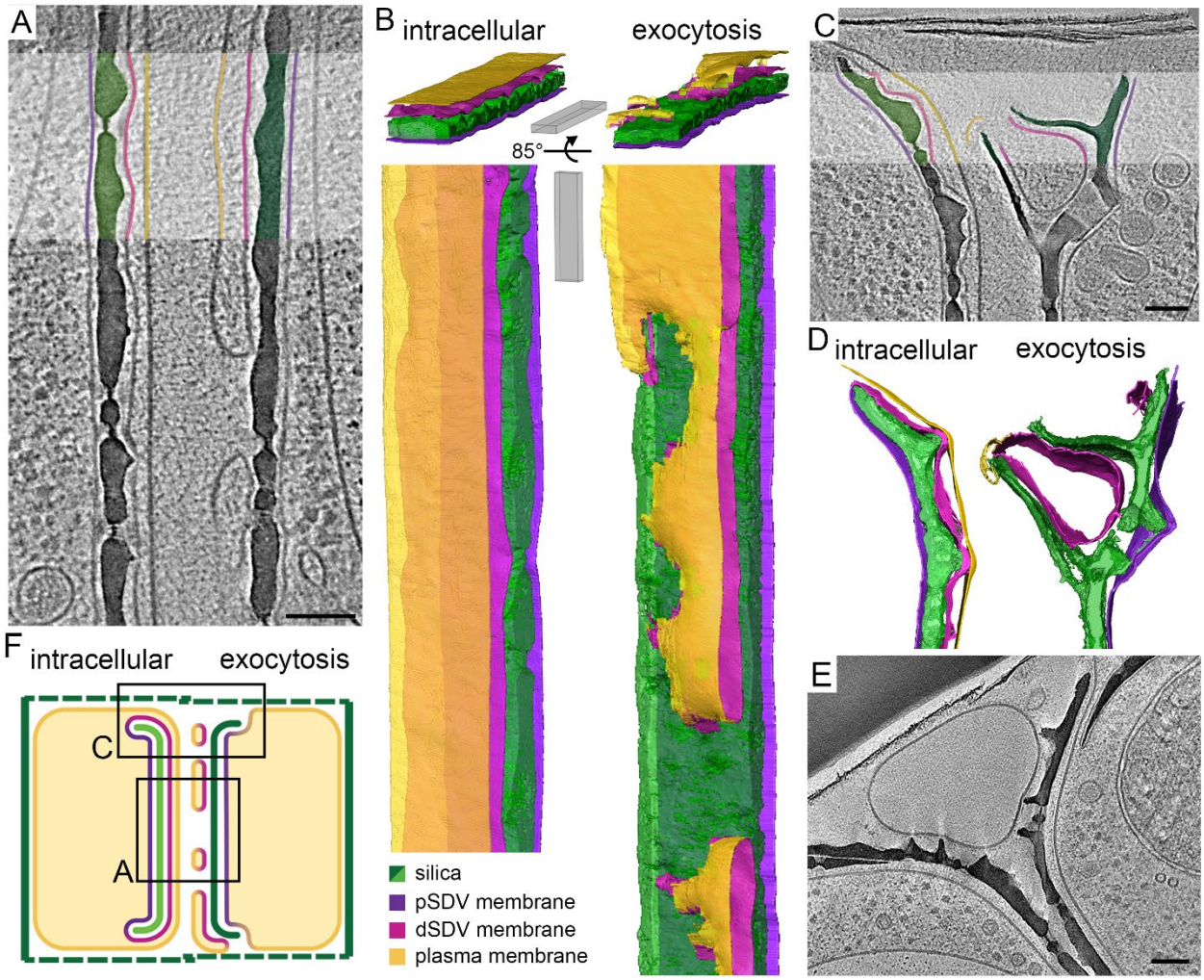

Figure 4. In-cell cryo-ET shows the native-state anatomy of valve exocytosis in *T. pseudonana*. (**A, C, E**) Slices through reconstructed 3D volumes; some features in the highlighted rectangles are artificially colored according to the color code in B. (**B, D**) Three-dimensional surface rendering of segmented volumes. (**F**) Schematic showing the proposed valve exocytosis mechanism of diatoms. **A** and **C** show different locations on the same daughter cells, indicated in **F**. Scale bars: 100 nm, slice thickness 1.15 to 5.7 nm. See also Movies S2-3.

262 **Discussion**

263 Extrusion of the rigid cell walls of diatoms is an exceptional exocytosis event, difficult to reconcile
264 with known exocytosis mechanisms. Our observations, of detached membrane patches in the
265 extracellular space of two diatom species acquired with three microscopy techniques, are
266 incompatible with classical exocytosis mechanisms. The structural characteristics of these
267 unconnected and loose membranes after valve formation is in sharp contrast to the SDV
268 ultrastructure during silica growth, which forms a highly confined space that is pivotal in
269 controlling the shape of growing silica structures (35–37). Therefore, we suggest that exocytosis
270 of mature valves occurs via a unique mechanism in which the old plasma membrane and distal
271 SDV membrane are discarded in the extracellular space and the proximal SDV membrane takes
272 the role of a new plasma membrane (Fig. 4F, Fig. S2). This scenario is in agreement with previous
273 observations of rapid exchange of SDV proteins with the plasma membrane in live-cell studies of
274 *T. pseudonana* (2, 38).

275 This scenario is also supported by the fact that none of the cells in our datasets show signs
276 of processing or recycling of the SDV membranes, or the formation of a new plasma membrane
277 under the valve. Nevertheless, we are aware that our live-cell imaging might not have the spatial
278 resolution to detect such events, and that electron microscopy only gives information on random
279 snapshots in time and space. For these reasons, we conducted a statistical analysis to determine
280 the probability that exocytosis does involve the endocytic recycling of the SDV membrane. The
281 tested scenario was that the ~1μm invaginations observed in *S. turris* are actually part of such
282 endocytic retrieval process (Fig. S7). If this is the case, it will require the recycling of ~1300 such
283 invaginations. We ran a statistical simulation, assuming a 10 seconds time window for an
284 invagination to develop and be visible in an image, and a total 30 minutes for valve exocytosis.
285 The simulation also addresses the probability to 'catch' this event in a random TEM thin slice (see
286 supplementary material for simulation description). Running the simulation for 10,000 times
287 showed that in more than 99.5% of the cases, the simulated scenario included the detection of
288 more than 7 such events when 68 observations were made (corresponding to the 68 actual
289 observations, Fig. 3). Therefore, we can rule out the option of internalization of these membranes

290 through compensatory endocytosis with a probability of $p<0.001$, according to the permutation
291 test.

292 The proposed scenario suggests that upon exocytosis the proximal SDV membrane
293 becomes the new plasma membrane. As the SDV and plasma membranes carry out specialized,
294 different tasks, it is likely that both require unique lipid and protein compositions, which would
295 need to be adjusted after fusion (39). The finding that the distal membranes disintegrate
296 extracellularly is surprising, as it seems wasteful to discard such a large amount of membranes
297 each cell cycle. The low affinity of FM4-64 to degrading debris precludes the ability to follow the
298 fate of these membranes (32). Nevertheless, it is important to note that the girdle bands form a
299 quasi-enclosed compartment around the newly formed valves, possibly slowing down diffusion
300 away from the cell and facilitating the uptake of the membrane debris for cellular use after
301 disintegration. This can conceivably minimize the energetic costs of such process.

302 The exocytosis of large content was also investigated in other organisms, demonstrating
303 mechanisms that differ from the classical secretory pathway of numerous small vesicles that fuse
304 with the membrane (40). One alternative is the exocytosis of giant vesicles in the *Drosophila*
305 salivary glands that squeeze out their viscous cargo through a pore by crumpling of the vesicular
306 membrane, followed by membrane recycling (41). Another alternative, the acrosome reaction,
307 surprisingly shares similarities with our proposal for diatom valve exocytosis. In this process, the
308 plasma membrane and distal acrosomal membrane fuse at several locations forming vesicles that
309 are dispersed in the environment while the proximal acrosomal membrane remains intact and
310 becomes the new boundary that separates the spermatozoa from the environment (42, 43).

311 To conclude, this work proposes a unique mechanism for the exocytosis of diatom silica,
312 which involves two remarkable events. First, the repurposing of an organelle membrane into a
313 plasma membrane and second, large-scale disintegration of membranes. This mechanism is
314 shared by two model diatom species, indicating that this might be a general mechanism. With the
315 toolbox for genetic research in diatoms growing, it will soon be possible to investigate the protein
316 machinery that is involved in the regulation of this event, and its relation to classical exocytosis.

317 **Acknowledgements**

318 We thank Anne Jantschke, Nathalie Pytlik, and Eike Brunner from TU Dresden for providing
319 cultures. We thank Simon Michaeli from the Volcani Institute (ARO) for his contribution in finding
320 the right live-cell imaging platform. Live-cell imaging was conducted at the de Picciotto Cancer
321 Cell Observatory In Memory of Wolfgang and Ruth Lesser. This project has received funding from
322 the European Research Council (ERC) under the European Union's Horizon 2020 research and
323 innovation programme (grant agreement No. 848339). D. dH. was supported by the Sustainability
324 and Energy Research Initiative (SAERI) of Weizmann Institute of Science.

325 **Data availability**

326 All source data generated or analyzed during this study will been deposited to Dryad.

327 **Competing interests**

328 The authors declare no competing interests.

329 **References**

330 1. N. Kroger, N. Poulsen, Diatoms — From Cell Wall Biogenesis to Nanotechnology. *Annu.*
331 *Rev. Genet.* **42**, 83–107 (2008).
332 2. A. Kotzsch, *et al.*, Silicanin-1 is a conserved diatom membrane protein involved in silica
333 biomineralization. *BMC Biol.* **15** (2017).
334 3. N. Kröger, R. Deutzmann, M. Sumper, Polycationic peptides from diatom biosilica that
335 direct silica nanosphere formation. *Science (80-.).* **286**, 1129–1132 (1999).
336 4. M. Sumper, E. Brunner, G. Lehmann, Biomineralization in diatoms: Characterization of
337 novel polyamines associated with silica. *FEBS Lett.* **579**, 3765–3769 (2005).
338 5. M. Hildebrand, Diatoms, Biomineralization Processes , and Genomics. *Chem. Rev.* **108**,
339 4855–4874 (2008).
340 6. R. W. Drum, H. S. Pankratz, Post mitotic fine structure of Gomphonema parvulum. *J.*
341 *Ultrasructure Res.* **10**, 217–223 (1964).

342 7. C. Heintze, *et al.*, An intimate view into the silica deposition vesicles of diatoms. *BMC*
343 *Mater.* **2**, 1–15 (2020).
344 8. B. Mayzel, L. Aram, N. Varsano, S. G. Wolf, A. Gal, Structural evidence for extracellular
345 silica formation by diatoms. *Nat. Commun.* **12**, 1–8 (2021).
346 9. M. Hildebrand, S. J. L. Lerch, R. P. Shrestha, Understanding Diatom Cell Wall Silicification
347 — Moving Forward. *Front. Mar. Sci.* **5**, 1–19 (2018).
348 10. N. Kröger, S. Lorenz, E. Brunner, M. Sumper, Self-assembly of highly phosphorylated
349 silaffins and their function in biosilica morphogenesis. *Science (80-.).* **298**, 584–586
350 (2002).
351 11. A. Scheffel, N. Poulsen, S. Shian, N. Kröger, Nanopatterned protein microrings from a
352 diatom that direct silica morphogenesis. *Proc. Natl. Acad. Sci.* **108**, 3175–3180 (2011).
353 12. M. Montagna, *et al.*, Interactions of long-chain polyamines with silica studied by
354 molecular dynamics simulations and solid-state NMR spectroscopy. *Langmuir* **36**, 11600–
355 11609 (2020).
356 13. A. Jantschke, *et al.*, Insight into the Supramolecular Architecture of Intact Diatom Biosilica
357 from DNP-Supported Solid-State NMR Spectroscopy. *Angew. Chemie Int. Ed.* **54**, 15069–
358 15073 (2015).
359 14. E. F. Stoermer, H. S. Pankratz, C. C. Bowen, Fine Structure of the Diatom Amphipleura
360 pellucida. II. Cytoplasmic Fine Structure and Frustule Formation. **52**, 1067–1078 (1965).
361 15. N. H. Battey, N. C. James, A. J. Greenland, C. Brownlee, Exocytosis and Endocytosis. *Plant*
362 *Cell* **11**, 643–659 (1999).
363 16. D. Schulz, Das Schicksal von Silicalemma und Plasmalemma während der Zellwandbildung
364 bei Coscinodiscus granii Gough und Thalassiosira eccentrica (Ehrenb.) Cleve. *Ber. Dtsch.*
365 *Bot. Ges.* **97**, 411–419 (1984).
366 17. B. E. Volcani, “Cell Wall Formation in Diatoms: Morphogenesis and Biochemistry” in
367 *Silicon and Siliceous Structures in Biological Systems*, (Springer, 1981), pp. 157–200.
368 18. Y. D. Bedoshvili, *et al.*, Frustule morphogenesis of raphid pennate diatom Encyonema
369 ventricosum (Agardh) Grunow. *Protoplasma* **255**, 911–921 (2018).

370 19. M. L. Chiappino, B. E. Volcani, Studies on the Biochemistry and Fine Structure of Silicia
371 Shell Formation in Diatoms VII. Sequential Cell Wall Development in the Pennate Navicula
372 pelliculosa. *Protoplasma* **93**, 205–221 (1977).
373 20. R. M. Crawford, Valve Formation in Diatoms and the Fate of the Silicalemma and
374 Plasmalemma. *Protoplasma* **106**, 157–166 (1981).
375 21. P. A. Dawson, Observations on the structure of some forms of Gomphonema Parvulum
376 Kutz. III. Frustule formation. *J. Phycol.* **9**, 353–365 (1973).
377 22. B. E. F. Reimann, J. C. Lewin, B. E. Volcani, Studies on the Biochemistry and fine structure
378 of silica shell formation in diatoms I. The Structure of the Cell Wall of Cylindrotheca
379 fusiformis. *J. Cell Biol.* **24**, 39–55 (1965).
380 23. A.-M. M. Schmid, Wall Morphogenesis in Coscinodiscus wailesii. *8th Diatom Symp.*, 293–
381 314 (1984).
382 24. C. W. Li, B. E. Volcani, Studies on the Biochemistry and Fine Structure of Silica Shell
383 Formation in Diatoms. X Morphogenesis of the Labiate Process in Centric Diatoms.
384 *Protoplasma* **124**, 147–156 (1985).
385 25. P. Gröger, N. Poulsen, J. Klemm, N. Kröger, M. Schlierf, Establishing super-resolution
386 imaging for proteins in diatom biosilica. *Sci. Rep.* **6**, 1–8 (2016).
387 26. P. G. Kroth, *et al.*, Genome editing in diatoms: achievements and goals. *Plant Cell Rep.* **37**,
388 1401–1408 (2018).
389 27. V. A. Chepurnov, *et al.*, In search of new tractable diatoms for experimental biology.
390 *BioEssays* **30**, 692–702 (2008).
391 28. H. A. von Stosch, G. Drebes, Entwicklungsgeschichtliche Untersuchungen an zentrischen
392 Diatomeen IV. *Helgoländer Wissenschaftliche Meeresuntersuchungen* **11**, 209–257
393 (1964).
394 29. Y. Kadan, *et al.*, In situ electron microscopy characterization of intracellular ion pools in
395 mineral forming microalgae. *J. Struct. Biol.* **210**, 107465 (2020).
396 30. M. Turk, W. Baumeister, The promise and the challenges of cryo-electron tomography.
397 *FEBS Lett.* **594**, 3243–3261 (2020).

398 31. K. Shimizu, Y. Del Amo, M. A. Brzezinski, G. D. Stucky, D. E. Morse, A novel fluorescent
399 silica tracer for biological silicification studies. *Chem. Biol.* **8**, 1051–1060 (2001).
400 32. S. Bolte, *et al.*, FM-dyes as experimental probes for dissecting vesicle trafficking in living
401 plant cells. *J. Microsc.* **214**, 159–173 (2004).
402 33. S. F. Kühn, C. Brownlee, Membrane organisation and dynamics in the marine diatom
403 Coscinodiscus wailesii (Bacillariophyceae). *Bot. Mar.* **48**, 297–305 (2005).
404 34. M. Schaffer, *et al.*, Optimized cryo-focused ion beam sample preparation aimed at in situ
405 structural studies of membrane proteins. *J. Struct. Biol.* **197**, 73–82 (2017).
406 35. B. Tesson, M. Hildebrand, Extensive and intimate association of the cytoskeleton with
407 forming silica in diatoms: Control over patterning on the meso- and micro-scale. *PLoS One*
408 **5** (2010).
409 36. A. M. L. Van de Meene, J. D. Pickett-Heaps, Valve morphogenesis in the centric diatom
410 Proboscia alata Sundstrom. *J. Phycol.* **38**, 351–363 (2002).
411 37. A. M. M. Schmid, Aspects of morphogenesis and function of diatom cell walls with
412 implications for taxonomy. *Protoplasma* **181**, 43–60 (1994).
413 38. D. P. Yee, M. Hildebrand, M. Tresguerres, Dynamic subcellular translocation of V-type H+-
414 ATPase is essential for biomineralization of the diatom silica cell wall. *New Phytol.* **225**,
415 2411–2422 (2020).
416 39. J. C. M. Holthuis, A. K. Menon, Lipid landscapes and pipelines in membrane homeostasis.
417 *Nature* **510**, 48–57 (2014).
418 40. E. D. Gundelfinger, M. M. Kessels, B. Qualmann, Temporal and spatial coordination of
419 exocytosis and endocytosis. *Nat. Rev. Mol. Cell Biol.* **4**, 127–139 (2003).
420 41. K. Kamalesh, *et al.*, Exocytosis by vesicle crumpling maintains apical membrane
421 homeostasis during exocrine secretion. *Dev. Cell* **56**, 1603-1616.e6 (2021).
422 42. M. Okabe, “The Acrosome Reaction: A Historical Perspective” in *Sperm Acrosome*
423 *Biogenesis and Function During Fertilization*, M. G. Buffone, Ed. (Springer International
424 Publishing, 2016), pp. 1–13.
425 43. C. N. Tomes, “Acrosomal Exocytosis” in *Molecular Mechanisms of Exocytosis*, (Springer

426 New York, 2007), pp. 117–147.
427 44. A. E. Weston, H. E. J. Armer, L. M. Collinson, Towards native-state imaging in biological
428 context in the electron microscope. *J. Chem. Biol.* **3**, 101–112 (2010).
429 45. W. J. H. Hagen, W. Wan, J. A. G. Briggs, Implementation of a cryo-electron tomography
430 tilt-scheme optimized for high resolution subtomogram averaging. *J. Struct. Biol.* **197**,
431 191–198 (2017).
432 46. D. N. Mastronarde, Automated electron microscope tomography using robust prediction
433 of specimen movements. *J. Struct. Biol.* **152**, 36–51 (2005).
434 47. J. R. Kremer, D. N. Mastronarde, J. R. McIntosh, Computer visualization of three-
435 dimensional image data using IMOD. *J. Struct. Biol.* **116**, 71–76 (1996).
436 48. A. Martinez-Sanchez, I. Garcia, S. Asano, V. Lucic, J. J. Fernandez, Robust membrane
437 detection based on tensor voting for electron tomography. *J. Struct. Biol.* **186**, 49–61
438 (2014).
439 49. W. Kukulski, M. Schorb, M. Kaksonen, J. A. G. Briggs, Plasma membrane reshaping during
440 endocytosis is revealed by time-resolved electron tomography. *Cell* **150**, 508–520 (2012).
441 50. M. Ginzburg, B. Z. Ginzburg, R. Wayne, Ultrarapid endocytotic uptake of large molecules
442 in Dunaliella species. *Protoplasma* **206**, 73–86 (1998).
443 51. T. J. Nawara, *et al.*, Imaging vesicle formation dynamics supports the flexible model of
444 clathrin-mediated endocytosis. *Nat. Commun.* **13**, 1–14 (2022).
445 52. A. Johnson, G. Vert, Single event resolution of plant plasma membrane protein
446 endocytosis by TIRF microscopy. *Front. Plant Sci.* **8**, 1–11 (2017).
447 53. D. Schulz, Das Schicksal von Silicalemma und Plasmalemma während der Zellwandbildung
448 bei Coscinodiscus granii Gough und Thalassiosira eccentrica (Ehrenb.) Cleve. *Ber. Dtsch.*
449 *Bot. Ges.* **97**, 411–419 (1984).
450

451 # Supplementary information

452

453 **Materials and methods**

454 *Cell cultures*

455 *S. turris* was isolated from the North Sea in 2004 and provided by the group of Prof. Eike Brunner,
456 TU Dresden. Diatom cultures were maintained in natural Mediterranean seawater that was
457 filtered, its salinity corrected to 3.5% and supplemented with f/2 nutrient recipe, and for
458 *Thalassiosira pseudonana* (CCMP1335) supplemented with 330 µM silicic acid. Cultures were
459 maintained at 18°C under 16/8 hours light/dark cycles.

460 *Cell cycle synchronization*

461 For synchronization of the cell cycle, 5 ml of a mature *S. turris* cell culture was used to start a new
462 50 ml culture. After 48 hours of growth under the normal 16L/8D cycle, the culture was placed in
463 darkness for 20 hours. After 20 hours of darkness, the culture was again exposed to light. *T.*
464 *pseudonana* synchronization was done using Si starvation, as previously described (7). To
465 maintain the culture in an exponential growth phase they were grown under 12/12 hours
466 light\dark cycles and diluted (1:10) into fresh medium every other day during the week before
467 culture synchronization. To induce Si starvation, 100 ml aliquots of culture were centrifuged at
468 3000 g for 10 min and re-suspended in Si-free artificial seawater or filtered seawater; this step
469 was repeated three times. The cultures (~0.5 million cells/ml), were then maintained in dark for
470 12 hours under agitation in a Si free medium to arrest the cell cycle. Then cultures were
471 transferred to continuous light for an additional 4 hours of Si starvation. At the end of the Si
472 starvation period, cells were concentrated to about 10 million cells/ml and Si was replenished to
473 330 µM. To track the formation of new silica, PDMPO [2-(4-pyridyl)-5-((4-(2-dimethylaminoethyl-
474 amino-carbamoyl)methoxy)-phenyl) oxazole] (ThermoFisher Scientific, USA) was added. PDMPO
475 fluorescence was monitored by imaging the cultures with an epifluorescence microscope (Nikon

476 Eclipse Ni-U, ex: 365 em: 525). Highest amount of dividing *S. turris* and *T. pseudonana* cell were
477 counted after 9 and 3 hours, respectively.

478 *Sample preparation for SEM*

479 Cells were prepared for SEM using critical point drying (CPD). Cells were fixed in a solution of 2%
480 Glutaraldehyde and 4% Paraformaldehyde in artificial seawater for 1 hour at room temperature
481 while shaking. After 3 washes with deionized water (Milli-Q® IQ 7003 Ultrapure Lab Water
482 System, Merck), the cells were dehydrated by washing in a graded series of ethanol. The final
483 wash was done in 100% anhydrous ethanol overnight. The dehydrated samples were then dried
484 in a critical point dryer using liquid CO_2 as transitional fluid. Dried cells were placed onto a
485 conductive carbon tape on an aluminium stub.

486 *SEM imaging*

487 Samples were sputter-coated with 2.5 nm (*T. pseudonana*) or 4 nm (*S. turris*) iridium (Safematic)
488 and imaged with an Ultra 55 FEG scanning electron microscope (Zeiss, Germany), using 3-5 kV,
489 aperture size 20-30 um and a working distance of about 3 mm.

490 *Live-cell imaging*

491 For single-cell time-lapse imaging, a culture was synchronized and stained with PDMPO (330 µM).
492 About 8 hours after the end of light starvation, when most cells had gone through cytokinesis, an
493 aliquot of 100 µl was taken and FM4-64 (ThermoFisher Scientific, USA) was added to a final
494 concentration of 4-8 µM to stain the membranes. After adding the membrane dye, a 20 µl drop
495 was mounted on a microscope slide and covered with a glass coverslip, using dental wax as
496 spacer. The samples were visualized using a Leica TCS SP8-STED confocal microscope equipped
497 with a HCS PL APO 86x/1.20W motCORR objective. FM4-64 and chlorophyll autofluorescence
498 were acquired by white-light laser using 550 nm laser line (6% laser power) and 650 nm laser line
499 (7% laser power), respectively. PDMPO fluorescence was acquired using a 405 nm laser (5% laser
500 power). HyD-SMD detectors were used for PDMPO and FM4-64 with emission collection width

501 set to 474-530 and 608-640 nm, respectively. Chlorophyll autofluorescence emission was
502 collected using a HyD detector with 741-779 nm detection width and the transmission channel
503 was detected with a PMT detector. The cells were imaged for 2 to 4 hours at intervals of 3 to 60
504 minutes. Images were analysed using Leica Application Suite X. In total, time lapses from over 50
505 cells were collected over the entire period.

506 *Sample preparation for TEM*

507 *S. turris* cells were cryo-fixed, using high pressure freezing (HPF), followed by freeze substitution
508 (FS), according to previously published protocols (29, 44). Synchronized cells were collected on a
509 5 µm filter membrane and transferred to an Eppendorf tube using 200 µl of seawater. After letting
510 the cells sediment for 10 minutes, 2 µl aliquots were pipetted into aluminium discs (Wohlwend
511 GmbH, Sennwald, Switzerland) and directly loaded into a Leica ICE high pressure freezing machine
512 (Leica Microsystems GmbH, Wetzlar, Germany). Concentrated diatom samples were vitrified in
513 liquid nitrogen (−192 °C) at 210 MPa (2048 bar). Vitrified samples were stored in liquid nitrogen
514 until freeze-substitution in an EM ASF2 (Leica Microsystems GmbH, Wetzlar, Germany). Vitrified
515 water was substituted with an organic solvent, 100% anhydrous acetone, at (−90 °C). Then,
516 acetone was supplemented with chemical fixatives (0.2% uranyl acetate and 0.2% osmium
517 tetroxide) to enhance cross-linking and contrast of cellular structures. The samples were
518 immersed in the solution for 48 hours at −90 °C and then allowed to gradually warm for 24 hours
519 to -20°C, and then in one hour to 0°C. After three washes in acetone, the acetone was replaced
520 with Epon (Agar Scientific Ltd, Stansted, U.K.) using gradient concentration mixtures (10%, 20%,
521 30%, 40%, 60%, 80%, 100% Epon in acetone), twice a day at room temperature. The sample in
522 100% Epon was hardened at 70 °C for 72 h. Ultrathin sections of 70 nm were sliced using an ultra-
523 microtome (Ultracut UCT, Leica Microsystems GmbH, Wetzlar, Germany) equipped with a
524 diamond knife (Ultra 45°, Diatome Ltd, Nidau, Switzerland). The sections were picked up onto
525 copper TEM grids, coated with carbon film. The sections were then post-stained by placing them
526 onto a drop of lead citrate solution. After three minutes of staining, the grids were washed three
527 times in drops of water and then dried by blotting onto whatman filter paper. In total, we

528 prepared 16 frozen samples that were further processed using freeze substitution during 3
529 different cycles, and subsequently imaged hundreds of cells.

530 *TEM imaging*

531 The TEM samples were imaged with a Tecnai Spirit TEM (FEI, Eindhoven, Netherlands) operated
532 at 120 kV and equipped with Gatan Oneview 4 k × 4 k camera (Gatan Inc., Pleasanton, U.S.A.).

533 *Plunge freezing*

534 Synchronized *T. pseudonana* cells were vitrified by plunge-freezing on glow discharged 200 mesh
535 copper R2/1 holey carbon film grids (Quantifoil Micro Tools GmbH, Grossloebichau, Germany). In
536 a Leica EM GP (Leica Microsystems GmbH, Wetzlar, Germany), 1 µl of artificial seawater was
537 pipetted on the copper side in order to enhance media flow to the blotting paper and 4 µl of cell
538 suspension at 7-13X10^6 cells/ml was pipetted on the carbon side. The grids were blotted for 6
539 seconds from the back side of the grid before they were plunged into a liquid ethane bath cooled
540 by liquid nitrogen.

541 *Cryo-FIB milling*

542 Vitrified cells were milled to thin lamellae with the Zeiss Crossbeam 550 FIB/SEM dual beam
543 microscope (Zeiss, Germany). The grids were coated with organometallic platinum by an *in situ*
544 Gas Injection System. The lamellae were milled at a 12º tilt relative to the grid plane with the
545 rough milling (to 1 µm thickness) involving 2 steps using the Ga^+ beam at a current of 750 pA and
546 300 pA. After rough milling all lamellae, they were thinned to 200 nm at a current of 50 pA.

547 *Cryo-electron tomography and volume rendering*

548 Cryo-electron tomography data were collected from 59 pairs of cells. The tilt series were acquired
549 using a Titan Krios G3i TEM (Thermo-Fisher Scientific, Eindhoven, The Netherlands), operating at
550 300 kV. Tilt series were recorded on a K3 direct detector (Gatan Inc., Pleasanton, U.S.A) installed
551 behind a BioQuantum energy filter (Gatan Inc., Pleasanton, U.S.A), using a slit of 20 eV. All tilt
552 series were recorded in counting mode at a nominal magnification of 33,000x, corresponding to

553 a physical pixel size of 0.26 nm, using the dose-symmetric scheme starting from the lamella pre-
554 tilt of -12º and with 2º increments (45). Tilt series appearing in Fig. 4 A and C were taken at 3 µm
555 defocus and using a Volta Phase Plate inserted. The tilt series range was between -60° to 50°. Tilt
556 series appearing in Fig. 4 E was taken at 7 µm defocus, an objective aperture of 100 µm inserted,
557 and -66° to 48° tilt range. Tilt series were acquired using an automated low dose procedure
558 implemented in SerialEM with a total dose set to ~100e-/Å2 (46). The tomograms were
559 reconstructed using IMOD software v. 4.9.12 (47). Amira software v2021.2 was used for
560 segmentation (Thermo-Fisher Scientific, Eindhoven, The Netherlands). Membranes were
561 segmented using the membrane enhancement filter module and manually refinement (48).

562 *Statistical simulations and analyses*

563 To test whether our data indeed indicate a novel exocytosis strategy rather than classical
564 exocytosis we ran simulations and 10000 permutations. In order to do so, we estimated how
565 many vesicles would have to be endocytosed to re-internalize a membrane equivalent in size to
566 the mature SDV of *S. turris* and simulated how many such vesicles should have appeared in our
567 dataset.

568 **SDV membrane surface area** (excluding the membranes around linking processes) ≈ Total plasma
569 membrane surface area ≈ surface area of a capsule

570 $$SA_{capsule} = 2\pi r(2r + a)$$

571

572 *S. turris* cells are 20 to 25 µm in diameter and 60 µm in length, so the surface area for an average
573 sized *S. turris* cell:

574 r =11 µm

575 a =40 µm

576 $SA_{capsule} \approx 4000\ \mu m^2$

577

578 **Membrane surface area of a vesicle**:

579 $$SA_{sphere} = 4\pi r^2$$

580

581 In our data we observed membrane invaginations of 0.5 to 1 µm. Membrane surface area of the
582 invaginations seen in *S. turris*:

583 r = 0.25 to 0.5 µm

584 SA_{sphere} = 0.78 μm^2 to 3.14 μm^2

585

586 **Number of vesicles to be endocytosed:**

587 If all of the membrane is endocytosed by vesicles of 0.5 µm:

588 4000/0.78 = 5128 vesicles

589 If all of the membrane is endocytosed by vesicles of 1 µm:

590 4000/3.14 = 1274 vesicles

591

592 **Chance of catching an endocytic vesicle in a TEM section:**

593 The chance of detecting a spherical vesicle of diameter x in a random slice going through the
594 round cross section of a cell with diameter y is

595 $$\frac{x}{y}$$

596 The chance to detect a vesicle of 1 µm in a TEM section of an *S. turris* cell of 25 µm is

597 $$\frac{1}{25}$$

598 The chance to detect a vesicle of 0.5 µm in a TEM section of an *S. turris* cell of 25 µm

599 $$\frac{1}{50}$$

600

601 **Duration of an endocytosis event for a 0.5-1 um vesicle:**

602 Studies of time resolved endocytosis indicate that a single endocytosis event of a vesicle with a
603 diameter of 0.5 µm should take at least 10 seconds. (49–52)

604

605 **Total duration of the exocytosis/endocytosis process:**

606 Based on our data, we surmise that the recycling process should be finished in 30 minutes.

607

608 Using the parameters described above we find that if compensatory endocytosis would take
609 place, we should see more than 7 vesicles in >99.5% of the cases.

610 The simulation was run in R, v. 4.1.2.

611

612 A histogram showing the frequency of simulations that detected each number of endocytic
613 vesicles during 68 observations. The two histograms show the two different vesicle sizes that
614 were simulated.

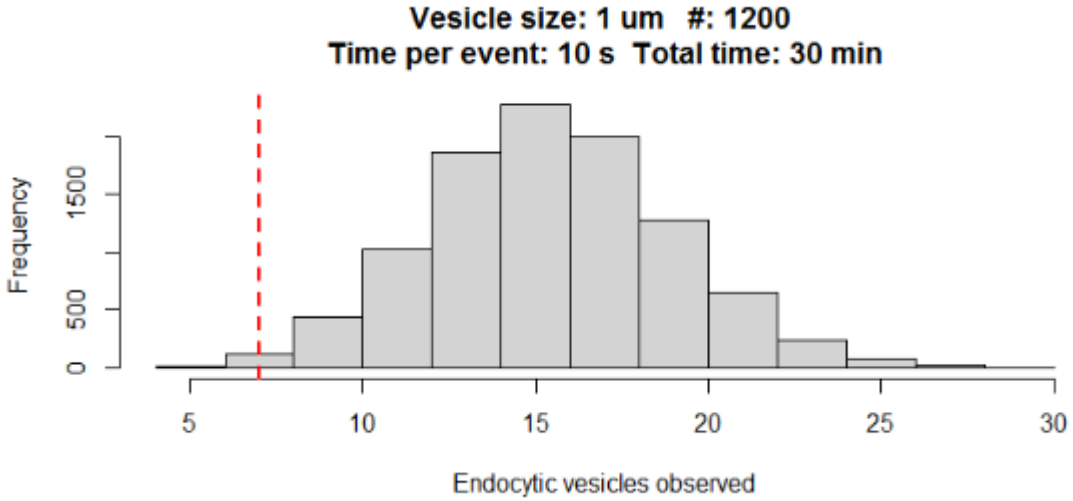

615

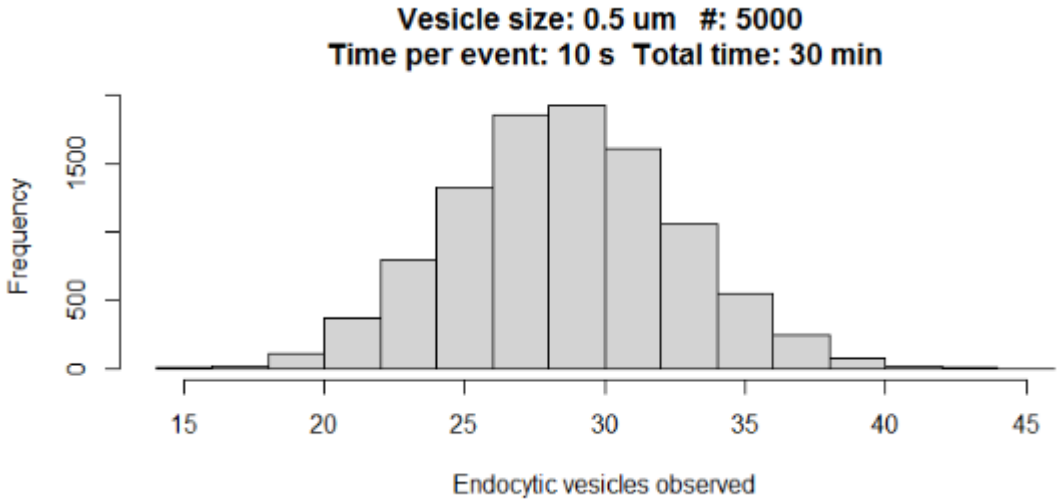

616

617

618

619

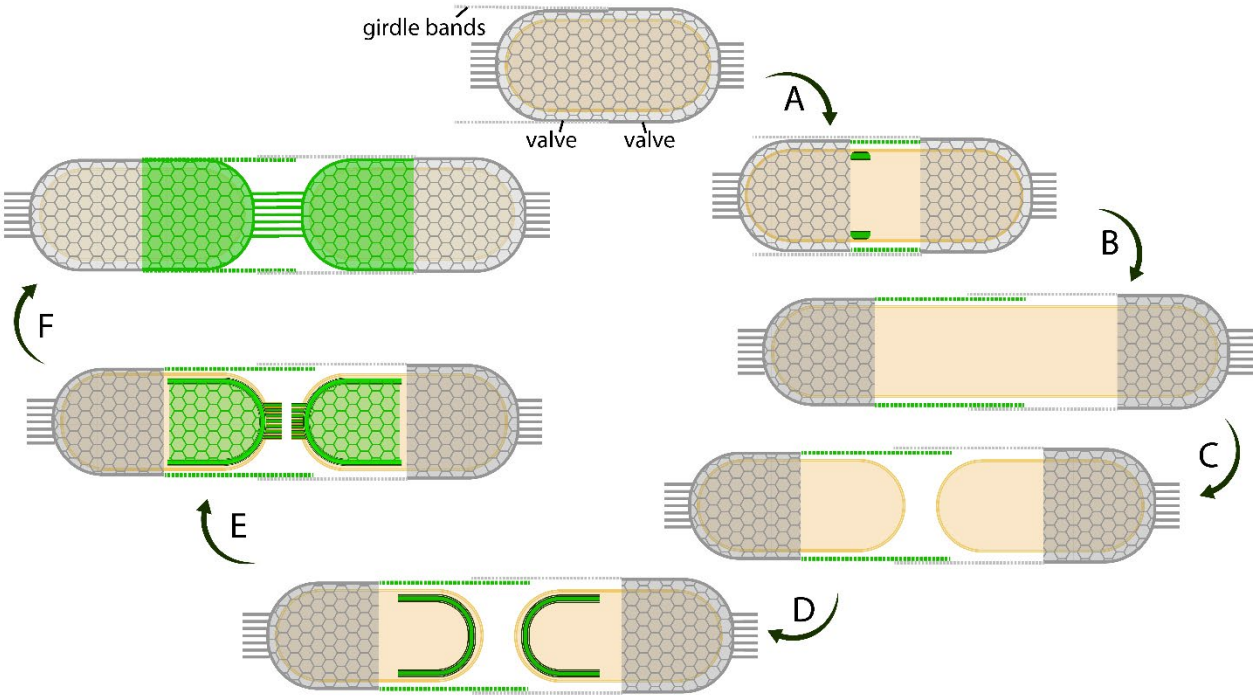

Figure S1. Cell cycle of *S. turris*. New silica elements, formed during the current cell cycle are colored green. Dashed lines represent girdle bands. (**A**) Start of a cell cycle with a protoplast enclosed by the two parental valves, the valve rims are directly adjacent to each other. The older valve is on the right, and the younger valve on the left. The younger valve is covered under the girdle bands of the older valve. (**B**) Protoplast starts growing in preparation for the next cell division. As the silica valves are rigid and not elastic, growth is only possible in longitudinal direction by pushing apart the two valves. New girdle bands (green) are formed in individual SDVs and added to the rim of the younger valve. (**C**) After the protoplast has reached its final length, the cell undergoes cytokinesis, resulting in two daughter cells enclosed in the parental cell wall. (**D**) Each daughter cell inherits one half of the parental cell wall and starts forming a new valve, inside an SDV, shortly after cell division. (**E**) The new valves are completed with attachment of the linking extensions, after which they are exocytosed. (**F**) Both daughter cells are now ready to continue to the next cell cycle.

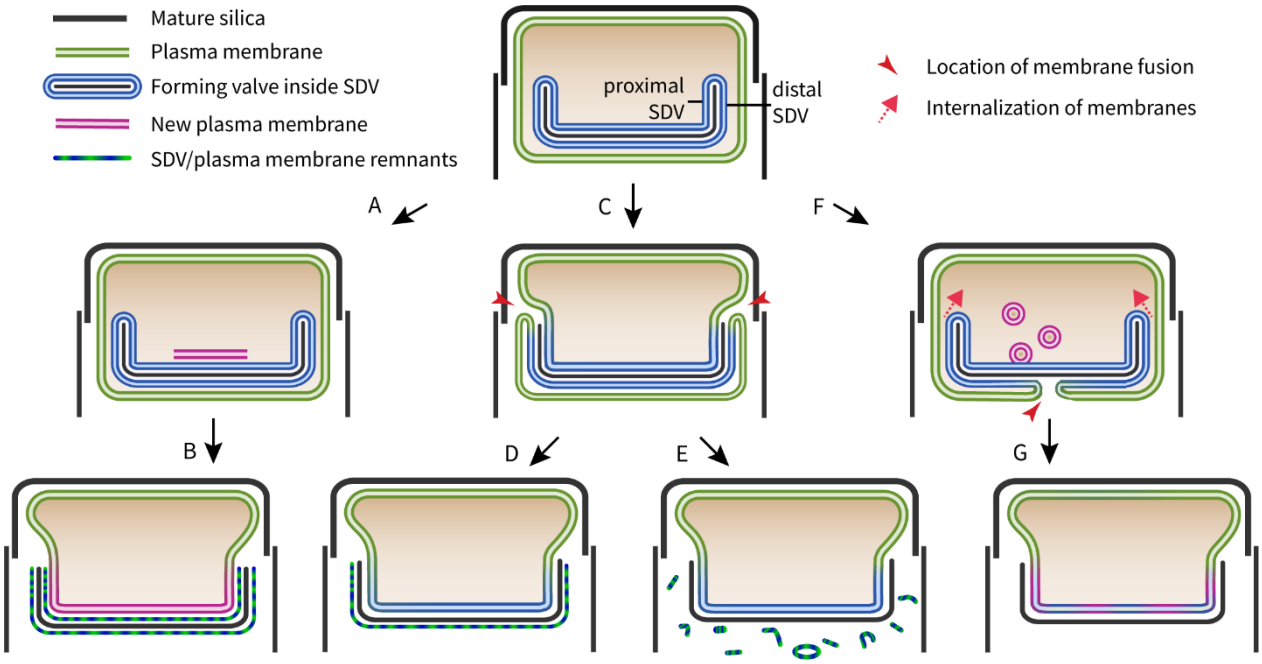

Figure S2. Hypotheses for valve exocytosis in diatoms. Early ultrastructural studies brought forward few models for silica cell wall exocytosis in diatoms that are reproduced here (14, 16–23). One scenario suggests that the newly formed valve is externalized through formation of a new plasma membrane underneath it (**A**). The SDV membrane and the original plasma membrane around the new valve remain in place, forming an organic layer around the silica (**B**). An alternative is that the valve is externalized as a result of localized fusion of the SDV and plasma membrane at the valve edge, such that the proximal part of the SDV membrane becomes the new plasma membrane (**C**). The distal part of the SDV membrane and the original plasma membrane were suggested to either shed off to the environment (**E**) or remain as an extracellular layer protecting the silica (**D**). The last model suggests localized membrane fusion at the apical part of the valve, followed by pulling of the distal SDV and original plasma membrane back into the cytoplasm at the valve edge (**F**). In this last model, which is in accordance with classical exocytosis, the composition of the proximal SDV membrane is altered for its new function as the plasma membrane (**G**). Our study support model C+E as the scenario for valve exocytosis.

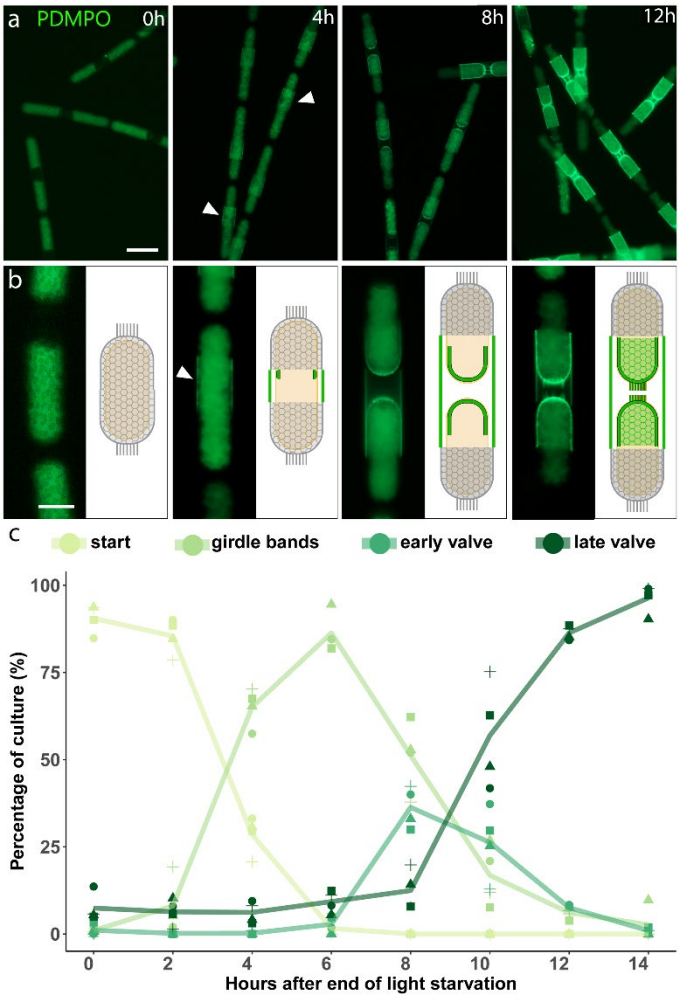

Figure S3. Light-induced synchronization of *S. turris* cell cycle. (**A**) Representative PDMPO fluorescence images of synchronized cultures. Elapsed time since the end of light starvation and addition of PDMPO is indicated in the image. Shortly after the end of light starvation, none of the cells have fluorescently labelled silica, only PDMPO fluorescence from within the vacuoles is visible. Four hours later, most cells have started forming girdle bands, visible as a fluorescent ring (arrowheads) around the cell. After eight hours, the majority of the culture is forming new, fluorescent valves. After twelve hours, nearly all cells have completed the formation of a new valve. Scale bar: 50 µm. (**B**) Key stages of cell wall formation: 'start', cells without PDMPO-labelled silica; 'girdle bands', cells during cell elongation and girdle band formation; 'early valve', after cell division, valve formation has started but is prior to growth of linking extensions; 'late valve', cells at later stages of valve formation when polygons and extensions are visible. Scale bar: 20 µm (**C**)

Percentage of cells at key stages during synchronized growth. The lines show the mean of four independent experiments, indicated with symbols. The highest percentage of cells that are forming valves is reached around nine hours.

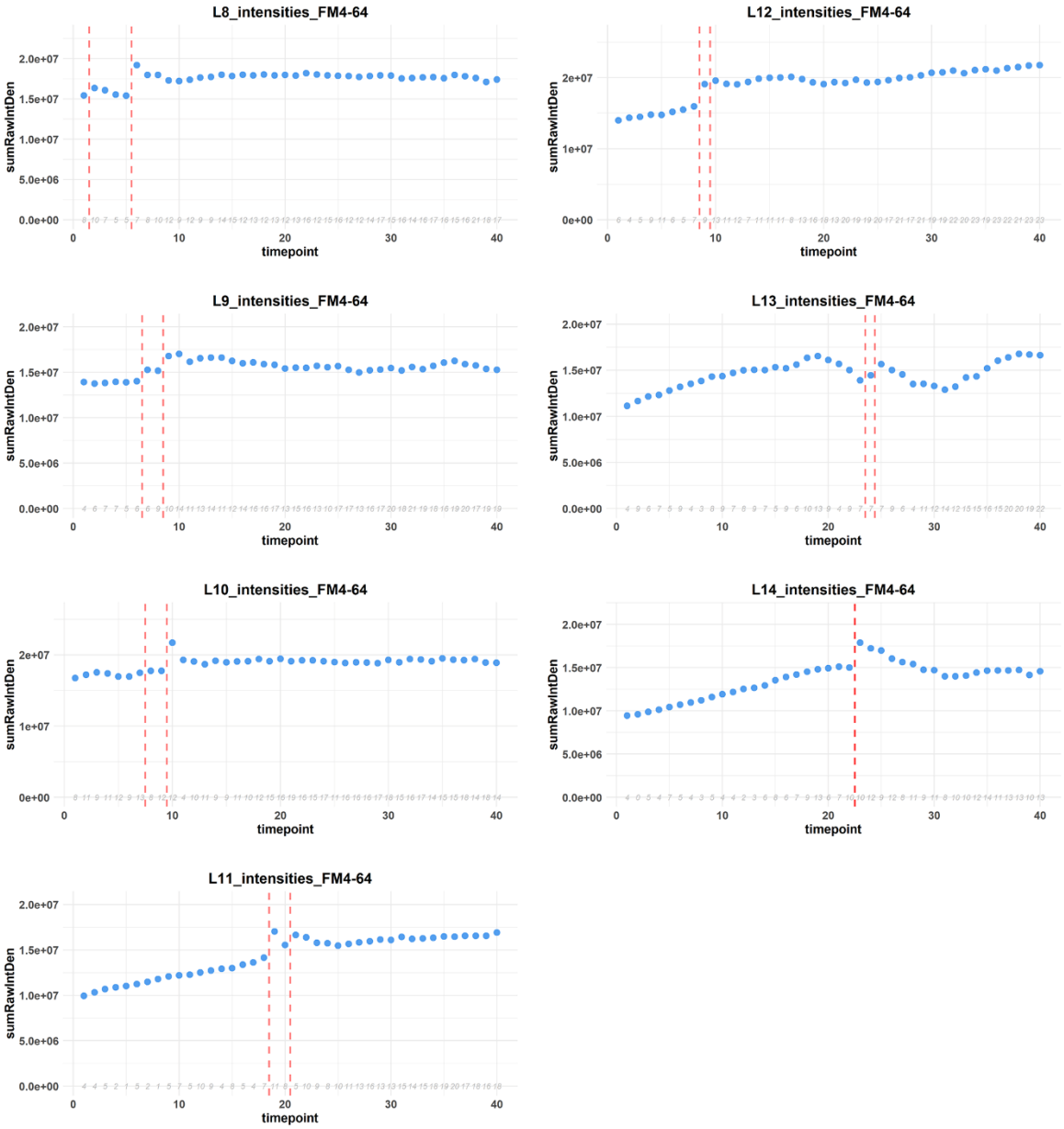

665 **Figure S4. FM4-64 fluorescence intensity during live-cell imaging.** Results from seven cells
666 undergoing valve formation and exocytosis are shown. Total FM4-64 fluorescence intensity
667 throughout time-lapses were measured using imageJ's 'raw integrated density (RawIntDen)'. This
668 measure gives the sum of all pixel intensities in an image. Here we plotted for each time point the
669 sum of RawIntDen of all slices in the z-stack. The red lines indicate where exocytosis happens,
670 based on loosening of the hexagonal pattern. Thus, in 6 out the 7 cells (except for L13) a clear
671 fluorescence increase is associated with the disappearance of the polygonal pattern. In L14 only
672 one of the two daughter cells remained in the field of view. Grey italic numbers indicate for each
673 time point the number of slices that contain one or more oversaturated pixels, the Z-stacks
674 contain 40 to 44 slices overall.

675

676

677

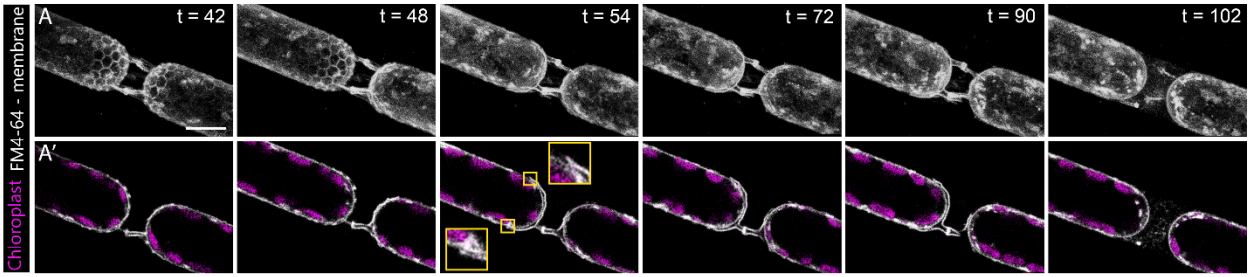

678 **Figure S5. Distal membranes that undergo degradation are disconnected from the cellular**
679 **membrane.** Representative (**A**) maximum intensity projections and (**A'**) single z-slices of time-
680 lapse confocal fluorescence images. Images show membrane staining (FM4-64) in white and
681 chloroplasts autofluorescence in magenta. The elapsed time since the start of imaging (in
682 minutes) is shown on the upper right corner. Exocytosis of the valve on the bottom right starts
683 between t=42 and t=48. The valve on the top left is exocytosed between t=48 and t=54. In t=54
684 to t=90, distal membranes around the valve are not connected to the cellular membrane. At t=102
685 the remnants have largely disintegrated. Scale bar: 10 µm.

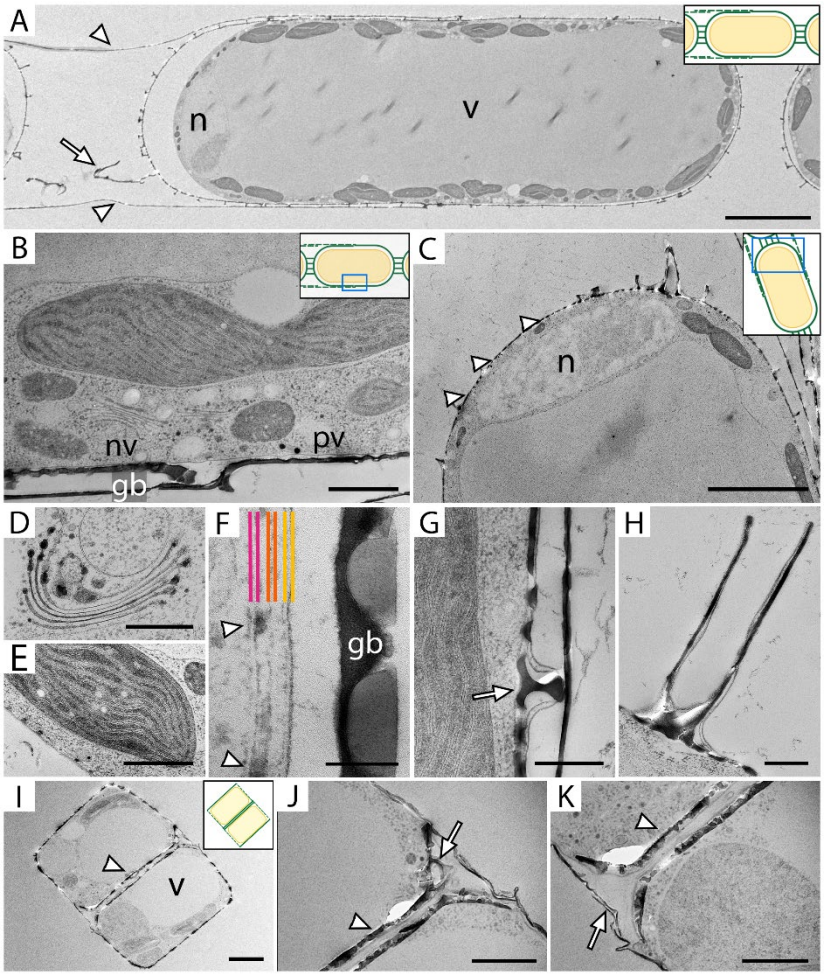

686 **Figure S6. Ultrastructural details of diatoms revealed by TEM imaging.** Insets indicate which part
687 of the cell is displayed. (**A**) A cross section through an entire cell, the nucleus (n), and the large
688 central vacuole (v) that is surrounded by darker chloroplasts are dominant. The silica cell wall
689 (dark contrast) is clearly visible at the left side, where the protoplast is not directly adjacent to
690 the cell wall due to slight plasmolysis. Arrowheads indicate girdle bands, and an arrow indicates
691 a linking extension. Scale bar: 10 µm. (**B**) The meeting point of a new valve (nv), and parental valve
692 (pv) with girdle bands (gb) attached to the latter. Scale bar: 1 µm. (**C**) Apex of a cell with the
693 nucleus (n) located directly under the valve. Silica protrusions indicated with arrowheads are
694 cross sections of the polygonal layer. Scale bar: 5 µm. (**D-H**) High magnification images of: (**D**)
695 Golgi-body. Scale bar: 500 nm. (**E**) Chloroplast. Scale bar: 1 µm. (**F**) SDV with growing silica
696 (arrowheads). Bilayers of the proximal SDV membrane (pink), distal SDV membrane (orange), and

697 plasma membrane (yellow) can be distinguished. Scale bar: 100 nm. (**G**) Fully formed polygon
698 (arrow) still inside an SDV. Scale bar: 500 nm. (**H**) Linking extension during its formation in an SDV.
699 Scale bar: 500 nm. (**I**) Cross section of two *T. pseudonana* daughter cells with intracellular valves
700 (arrowheads). Scale bar: 1 µm. (**J-K**) Higher magnification of the cells in **I**, with arrow in **J** indicating
701 a fultoportula in the forming valve and arrow in **K** indicating parental girdle bands. Scale bars: 500
702 nm.

703

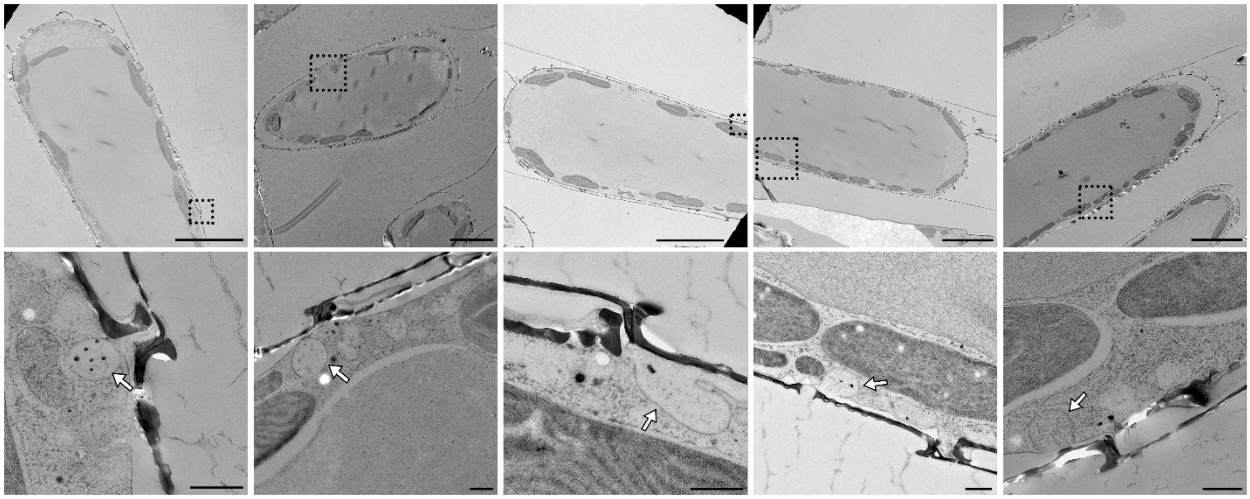

704 **Figure S7. Instances of membrane invagination during valve exocytosis.** Examples of cells that
705 are undergoing valve exocytosis, i.e. have a mature valve that is exposed to the exterior but still
706 surrounded by membrane (remnants). The bottom row shows magnified views of the boxed areas
707 in the top row, arrows indicate membrane invaginations. Scale bars: 1 µm (top row) and 500 nm
708 (bottom row).

709

710 **Movie S1.** Time-lapse imaging video of *S. turris* cell, stained with FM4-64, during valve formation
711 and exocytosis. (MP4 2186 kb)

712 **Movie S2.** Animation of cryo-ET dataset of *T. pseudonana* shown in Figure 4 A. (MP4 51 Mb)

713 **Movie S3.** Animation of cryo-ET dataset of *T. pseudonana* shown in Figure 4 C (MP4 51 Mb)